MAUSAM, **77**, 3 (July 2026),1035-1046

MAUSAM

DOI: https://doi.org/10.54302/mausam.v77i3.6893
Homepage: https://mausamjournal.imd.gov.in/index.php/MAUSAM

UDC No.551.508.8:004.85:551.509.324

An LSTM based model for the prediction of INSAT-3DR satellite images for nowcasting

AMIT SAXENA[1], DAMODAR PATEL[1], ABHISHEK DUBEY[2], PRATIKSHA DUBEY[3], PANKAJ KUMAR[3,*] and ASHIM KUMAR MITRA[3]

[1]*Department of CSIT, Guru Ghasidas Vishwavidyalaya Bilaspur, Chhattisgarh, India,*

[2]*IT Department, University of Technology and Applied Sciences, Salalah, Oman,*

[3]*India Meteorology Department, New Delhi, India*

(*Received 11 November 2024, Accepted 7 March 2026*)

***Corresponding author's email: kumarpankaj2794@gmail.com**

सार – मौसम की विपरीततम परिस्थितियों की आवृत्ति और तीव्रता दोनों में वृद्धि के कारण विकट मौसम की घटनाओं के लिए सटीक और शीघ्र चेतावनी प्रणालियों की मांग बढ़ रही है। ऐसी विनाशकारी घटनाओं की सटीक अग्रिम भविष्यवाणी मौसम पूर्वानुमानकर्ताओं के लिए एक महत्वपूर्ण चुनौती बनी हुई है, जिससे आपदा न्यूनीकरण कठिन हो जाता है। तत्काल पूर्वानुमान की सटीकता बढ़ाने के लिए, मौसम संबंधी (रडार, सैटेलाइट और सतही अवलोकन) और भौगोलिक जानकारी (ऊंचाई, अनावरण, वनस्पति, जलवैज्ञानिक विशेषताएं और मानवजनित विशेषताएं) सहित कई डेटा स्रोतों को पूर्वानुमान ढाँचे में तेजी से एकीकृत किया जा रहा है। यह अध्ययन INSAT-3DR डेटा का उपयोग करके अल्पकालिक सैटेलाइट छवि पूर्वानुमान के लिए लॉन्ग शॉर्ट-टर्म मेमोरी (LSTM) न्यूरल नेटवर्क को नियोजित करने वाले एक डीप लर्निंग-आधारित आर्किटेक्चर को प्रस्तुत करता है, जो मौसम तत्काल पूर्वानुमान अनुप्रयोगों में एक महत्वपूर्ण भूमिका निभाता है। प्रायोगिक मूल्यांकन थर्मल इन्फ्रारेड-1 (TIR-1) चैनल का उपयोग करके किया गया है। LSTM-आधारित फ्रेमवर्क सैटेलाइट छवियों को 5 × 5, 20 × 20 और 50 × 50 रिज़ॉल्यूशन के पिक्सेल ब्लॉकों में यादृच्छिक रूप से खंडित करके संसाधित करता है। भविष्य की सैटेलाइट छवियों का 30 मिनट, 1 घंटे, 1.5 घंटे और 2 घंटे के अग्रिम समय (Lead times) पर पूर्वानुमान लगाने के लिए तीन मॉडल संस्करण–CNN-LSTM, द्विदिश (Bidirectional) LSTM और वैनिला (Vanilla) LSTM लागू किए गए हैं। TIR-1 बैंड के लिए सर्वश्रेष्ठ प्रदर्शन करने वाला मॉडल लगभग 1.40% की औसत सामान्यीकृत माध्य निरपेक्ष त्रुटि (Normalized mean absolute error) प्राप्त करता है, जो उच्च पूर्वानुमान सटीकता प्रदर्शित करता है और INSAT-3DR सैटेलाइट छवि तत्काल पूर्वानुमान के लिए प्रस्तावित दृष्टिकोण की प्रभावशीलता की पुष्टि करता है।

ABSTRACT. The demand for accurate and early warning systems for severe weather occurrences is increasing due to the growth in both the frequency and intensity of extreme meteorological phenomena. Accurate advance prediction of such catastrophic events remains a significant challenge for weather forecasters, making disaster mitigation difficult. To enhance nowcasting accuracy, multiple data sources including meteorological (radar, satellite, and surface observations) and geographical information (elevation, exposure, vegetation, hydrological characteristics, and anthropogenic features) are increasingly integrated into forecasting frameworks. This study, presents a deep learning–based architecture employing Long Short-Term Memory (LSTM) neural networks for short-term satellite image prediction using the INSAT-3DR data, which plays a crucial role in weather nowcasting applications. Experimental evaluation is carried out using the Thermal Infrared-1 (TIR-1) channel. The LSTM-based framework processes satellite imagery by randomly segmenting images into pixel blocks of 5 × 5, 20 × 20, and 50 × 50 resolutions. Three model variants CNN–LSTM, Bidirectional LSTM, and Vanilla LSTM are implemented to predict future satellite images at lead times of 30 minutes, 1 hour, 1.5 hours, and 2 hours. The best-performing model for the TIR-1 band achieves an average normalized mean absolute error of approximately 1.40%, demonstrating high prediction accuracy and confirming the effectiveness of the proposed approach for INSAT-3DR satellite image nowcasting.

Key words – Weather nowcasting, deep learning, long short-term memory, INSAT-3DR data, Satellite image prediction.

1. Introduction

The meteorologists have been facing one of the biggest challenges in predicting various extreme weather events accurately and in time to avoid disasters. Weather nowcasting (Lebedev *et al*., 2019)is the study that focuses on the analysis and prediction of weather prediction in the next 0 to 6 hours. It is becoming increasingly significant in risk prevention and crisis management. The historical meteorological data, including radar measurements, satellite data, and ground observations, are all accessible to consumers from meteorological institutes. Furthermore, weather satellites are constantly collecting data on temperature, winds, and clouds, and real-time data is being collected by radars and ground stations. Hence, machine learning (ML)(Bharill *et al*., 2020; Kamber *et al*., 2006) based algorithms may employ a large amount of data from various sources to enhance the effectiveness of weather prediction systems. There is a great chance to examine and precisely predict weather events because of the volume of data that can be analyzed and the desire for better nowcasting methods.

Recent methods for nowcasting utilize various kinds of data sources, such as geographical and meteorological information (elevation, exposure, vegetation, hydrological features, and anthropological features), which are important for accurate nowcasting. One type of satellite used for monitoring and climate is a weather satellite. The weather satellites are equipped with radiometers that measure electromagnetic radiation's radiant power and create images of the Earth in order to gather data. They detect either visible, infrared, or microwave radiation for the purpose of monitoring weather systems around the world. This equipment detects electrical voltages, which are then transformed into digital signals, transmitted to receiving stations on the ground, and finally transmitted to several weather forecast centres around the world.

Information on weather and ground conditions in regions that are not monitored by weather radars or other remote sensing systems, such as meteorological stations, can be obtained through satellite images, which is a valuable source of data for operational meteorology. Various types of sensors are used by weather satellites for collecting a wide range of data, such as temperature of the surface or cloud top, surface reflectance, moisture content in the middle and upper layers of the troposphere, ozone concentration, and high-resolution visible images, to mention a few. These parameters are collected and transmitted over various channels. By combining data from these channels, more information can be demonstrated than by using them individually. This leads to improved satellite images, which are highly helpful for nowcasting weather conditions up to twelve hours in advance. Operational meteorologists present all of these products as coloured maps that are simple to evaluate quickly. Each pixel on this type of map indicates a specific geographic place, and the colour of the pixel denotes a particular value for the product being displayed or a specific attribute of the atmosphere, soil, or ocean. Automated feature detection and prediction on satellite images is becoming a growing trend because of the vast number of weather satellite products and related features that have been identified, as well as the usual 5- to 15-minute collection frequency.

The weather nowcasting problem is often addressed with machine learning (Dubey and Saxena, 2017), and deep learning (DL)(Zhu *et al*., 2024) methods. Recently, a lot of advancement has been achieved in the field of DL-based weather nowcasting using data from satellite and radar sources. The Indian National Satellite System, or INSAT(INSAT-3DR | Meteorological and Oceanographic Satellite Data Archival Centre, n.d.), is a system of multifunctional geostationary satellites that India deployed in order to satisfy its requirements in meteorology, broadcasting, telecommunications, and search and rescue, launched in 1983. INSAT stands as the largest domestic communication network in the Asia-Pacific region. Since Indian Space Research Organization (ISRO) is part of the COSPAR-Sarsat program, the satellites also include transponders to receive distress alerts for search and rescue operations in the South Asian and Indian Ocean regions. In this research, INSAT-3DR satellite data are used.

Nowcasting is the crucial study in the present scenario, looking to a wide variation of weather throughout the world. This is the basic motivation for the present study. After an extensive literature review, it was noted that there have been similar studies with reference to the datasets belonging to different countries other than India. This was the major motivation behind starting this study. The present work focuses on LSTM-based modeling to explicitly learn the spatiotemporal evolution of cloud patterns.

The objective of this study is to develop an LSTM-based nowcasting framework using INSAT-3DR satellite imagery. To achieve this objective, the present study investigates the nowcasting of INSAT-3DR satellite data based on datasets provided by the India Meteorological Department (IMD). The application of the proposed methodology to INSAT-3DR data for short-term nowcasting represents the key novelty and uniqueness of this work.

The remaining part of the paper is organized as follows. The methods for weather forecasting based on

satellite data are reviewed in Section 2. Section 3 presents the proposed methodology. Section 4 provides the results and discussion. The conclusion and future work for further research are outlined in Section 5.

2. Data and methodology

2.1. *Literature review on weather forecast based on satellite data*

Over the past decades, a lot of work has been carried out to improve Numerical Weather Prediction (NWP) models for precipitation forecasts. Precipitation nowcasting based on spatiotemporal extrapolation (Kotsuki *et al*., 2019) was used to provide a better precipitation forecast at shorter lead times with much less computation. Space-time extrapolation was used by Otsuka *et al*. (2016) for satellite-based global precipitation, with data assimilation being performed to increase motion vector accuracy. Precipitation nowcasting using satellite-based global precipitation projections has proven to be valuable in areas without access to ground-based weather radar networks. Wang *et al*. (2020) compared observations of several satellite precipitation products (IMERG-E, IMERG-L, and IMERG-F) during a period of tropical cyclones in the Yangtze River Delta area of China. The authors demonstrated via the conducted tests the positive effects of using the most effective IMERG precipitation product together with traditional observation data integrated into the Weather Research and Forecasting (WRF) model for modelling heavy rainfall events that transpired across the area under study.

Most of the research that proposes machine-learning approaches for the nowcasting problem uses recurrent neural networks (RNN)-based learning models, usually with CNN elements as well. These models have the advantage of being able to optimize various relevant metrics very well, due to the time-series nature of the data and the models' inherent ability to learn from such data. An important disadvantage, however, is the need for powerful GPUs to be able to run such algorithms on a lot of data. Even with high end hardware, training times for training RNNs are very high.

In order to provide reliable predictions for areas without radar systems, (Lebedev *et al*., 2019) proposed a method for precipitation forecasting using satellite images. Their solution was integrated into Yandex. The proposed approach is a two-step process that involves first creating a precipitation map using satellite images and then utilizing the map to forecast future precipitation. An RNN-based model combined with a U-Net model and a combined loss function developed from the binary cross-entropy loss and the dice loss was used to carry out the precipitation detection phase. It has been found that using additional features improves detection, such as solar altitude, topographic maps, and numerical weather forecast information. Their U-Net model outperformed two physics-based approaches as well as a shallow convolutional neural network on the detection task.

Kumar *et al*. (2020) proposed the Convcast precipitation nowcasting architecture, which uses a ConvLSTM architecture to forecast several types of short-term precipitation occurrences using satellite data. To train the model, ten consecutive NASA IMERG precipitation data sets at 30-minute intervals were used. Precipitation forecasting with an accuracy of 0.93 is achieved by using the anticipated precipitation data frequently, up to 150 minutes in advance (Kumar *et al*., 2020). Recently, RNN-based techniques were tested by Berthomier *et al*. (2020) using Meteosat satellite data, demonstrating the better performance of the UNet-based strategy in different synergies between traditional RNNs, LSTMs, Conv-nets, and UNet. Due to the similarities in the time-series structure of the two forms of data, this is further reinforced by (Agrawal *et al*., 2019) for the nowcasting issue based on radar data, which is still pertinent for our use case.

Ionescu *et al*. (2021) introduced DeePSat, a CNN architecture designed for short-term satellite image prediction, aiding weather nowcasting. Experimental evaluation of data from EUMETSAT's Meteosat-11 satellite using five satellite products shows DeePSat's effectiveness with an average normalized mean absolute error of 3.84%, demonstrating its superior performance compared to similar approaches.

Shukla *et al*. (2010) proposed a novel image sequence extrapolation framework for near-real-time weather nowcasting using geostationary satellite images. The study developed and evaluated three models: spatio-temporal autoregressive (STAR), discrete Fourier transform (DFT), and a hybrid DFT–STAR method in the Asian monsoon area. Based on skill scores and performance indices, an optimal scheme combining STAR and hybrid DFT–STAR models was identified, demonstrating reliable image prediction up to a 3-hour forecast lead time under varying meteorological conditions.

Shukla *et al*. (2013) addressed limitations in satellite-based weather nowcasting arising from the inadequate representation of transitions between different meteorological structures. To improve nowcasting efficacy, they used a clustering methodology inside a spatiotemporal autoregressive regression framework,

enabling the modeling of unique spatiotemporal correlations for various cloud regimes. Experimental results over a large dataset demonstrated statistically significant improvements in forecast skill, including higher probability of detection (POD) and critical success index (CSI), along with reduced false alarm rates compared to unclassified and persistence-based predictions. The positive impact of clustering was most pronounced up to a 2-hour lead time, with notable improvement at 3 hours, highlighting the model's potential for real-time forecasting of convective systems.

Son and Thong (2017) introduced two hybrid weather nowcasting approaches using image fuzzy clustering, referred to as PFC-STAR and PFC-PFR. The PFC-STAR approach integrates picture fuzzy clustering with spatiotemporal autoregressive regression, while PFC-PFR integrates picture fuzzy clustering with picture fuzzy rule-based inference. Both methodologies include training processes to improve predictive accuracy. Experimental findings on satellite image sequences in Southeast Asia indicated that the proposed methods outperform other methods by adeptly handling uncertainties and transitions among various meteorological structures, demonstrating their suitability for short-term weather nowcasting.

Singh *et al*. (2023) emphasized the significance of satellite-based nowcasting for the Indian monsoon area, which exhibits significantly different rainfall patterns. They developed a Nowcasting of Extreme Orographic Rain (NETRA) model based on INSAT-3D/3DR, originally for the Western Himalayan area and then expanded to include the whole Indian subcontinent. The system delivers near-real-time heavy rainfall notifications at 30-minute intervals via the MOSDAC online platform. Validation over a two-year period using INSAT-3D/3DR Hydro–Estimator–based Quantitative Precipitation Estimates showed robust spatial and temporal rainfall detection capability. While overall QPE correlation was modest, the model showed high skill for heavy rainfall events ($r > 0.7$), probability of detection exceeding 95% during the monsoon season, low false alarm rates, and robust performance for extreme events as indicated by EDS, EDI, and SEDI indices, highlighting its significant societal relevance for disaster risk reduction in India.

2.2. *Methodology*

2.2.1. *Description of datasets*

INSAT-3DR satellite data by the IMD, Delhi Meteorological Administration and retrieved in HDF5 image format is used in the experiments. INSAT-3DR carries two instruments: the INSAT-3DR sounder and the INSAT-3DR imager. The INSAT-3DR sounder is a 19-channel sounder that aims to provide vertical profiles of temperature, humidity, and integrated ozone. The INSAT-3DR imager is a multispectral optical radiometer capable of image generation in six bands: one visible band (0.55–0.75 μm) and five infrared bands (1.55-1.70 μm (SWIR, Short Wave Infrared), 3.80–4.00 μm (MIR, MidWave Infrared), 6.50–7.10 μm (water vapor), 10.30–11.30 μm (TIR–1, Thermal Infrared-1), and 11.50–12.50 μm (TIR–2, Thermal Infrared-2)), the INSAT-3DR imager provides the ability to take images of the earth disc from geostationary altitude. Normally, the sub-satellite point's ground resolution is 1 km x 1 km for the visible and SWIR bands, 4 km x 4 km for one MIR and both TIR bands, and 8 km x 8 km for the water vapour band (Giri *et al*., 2023).

For each of the channels, the value range is between 0 and 1023, and image sampling distances of 4 km for all channels except the high-resolution visible, which is at 1 km, while the time resolution is 30 minutes. In this study, a subdomain of the Earth's full disk has been observed by the INSAT-3DR, an area approximately determined by a square with the South Asian and Indian Ocean Region.

The TIR-1 channel of INSAT-3DR is selected in this study for future image predictions at 30-minute, 1-hour, 1.5-hour, and 2-hour lead times because it provides continuous day-and-night observations and effectively captures cloud-top brightness temperature variations, which are critical indicators of cloud evolution and convective activity. Unlike visible channels, the TIR-1 channel is independent of solar illumination, making it particularly suitable for short-term nowcasting applications. Moreover, TIR-1 data exhibit strong temporal consistency and sensitivity to cloud dynamics, which are essential for learning spatiotemporal patterns using LSTM-based models. Consequently, the TIR-1 channel provides a reliable and physically meaningful input for accurate nowcasting. In Fig. 1, TIR-1 channel data are present in this image, and in this image, the total number of pixels is 1616x1618 (X-axis, Y-axis).

2.2.2. *LSTM model*

DL based models, LSTMs (Sherstinsky, 2020), are valuable tools for weather nowcasting due to their ability to capture complex temporal relationships and adapt to evolving weather patterns. They enhance the performance and reliability of short-term weather predictions. This study used three different variants of LSTM: Convolutional Neural Network–LSTM (CNN-LSTM) (Gao *et al*., 2023), Bidirectional LSTM (B-LSTM) (Venkatesan *et al*., 2022), and Vanilla LSTM (V-LSTM) (Sherstinsky, 2020).

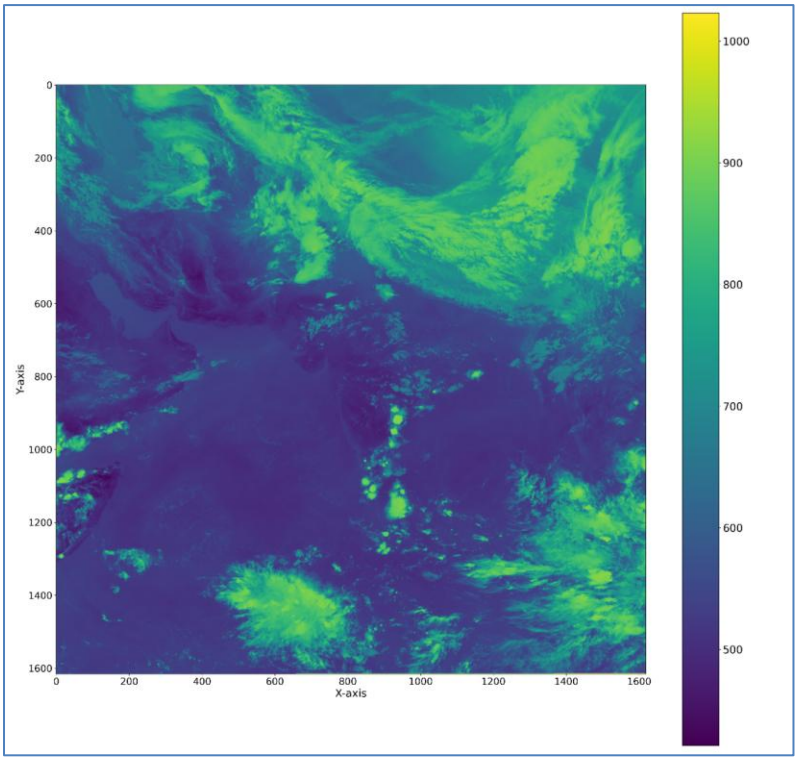

Fig. 1. A Sample Input Image on TIR-1 Data

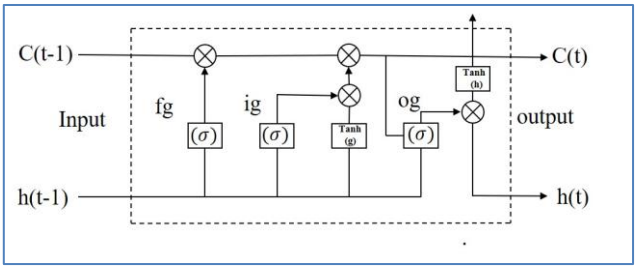

Fig. 2. Structure of Long Short-Term Memory

Long short-term memory (LSTM): LSTM is an RNN (Sherstinsky, 2020) architecture developed to overcome the vanishing gradient issue in regular RNNs. LSTM networks may learn long-term relationships in sequential data and are extensively used for natural language processing, speech recognition, and time-series prediction. The addition of a memory cell in the network enables it to selectively forget or retain information over time, making it well-suited for simulating sequential data with long-term dependencies.

The following equations illustrate the operation of an LSTM neuron architecture:

Forget gate,

$$fg = \sigma_a\left(W_{fg} \times x_t + U_{fg} \times h(t-1) + b_{fg}\right) \quad (1)$$

Input gate,

$$ig = \sigma_a(W_{ig} \times x_t + U_{ig} \times h(t-1) + b_{ig}) \quad (2)$$

Output gate,

$$og = \sigma_a(W_{og} \times x_t + U_{og} \times h(t-1) + b_{og}) \quad (3)$$

$$C'(t) = \sigma_h(W_{ct} \times x_t + U_{ct} \times h(t-1) + b_{ct}) \quad (4)$$

Cell state,

$$C(t) = fg.C(t-1) + ig.C'(t) \quad (5)$$

Hidden state,

$$h(t) = og.\sigma_h(C(t)) \quad (6)$$

where W_{fg}, W_{ig}, W_{og}, U_{fg}, U_{ig}, U_{og} are weight matrices, b_{fg}, b_{ig}, b_{og}, $b_{ct}$are bias and $x_t$is input

2.2.2.1. *CNN-LSTM*

CNNs and LSTM networks are combined in the CNN-LSTM hybrid neural network model to handle tasks requiring both temporal and spatial dependence. By using convolutional filters and pooling processes, CNNs have

expertise in extracting spatial features and patterns from data, including images or sequences. On the other hand, due to their special gating mechanisms that control the information flow, LSTMs are excellent at detecting and retaining long-term dependencies in sequential data.

In the CNN-LSTM architecture, the convolutional layers analyze the input data in order to extract spatial information. Then, in order to decrease dimensionality while keeping crucial data, these features are processed through pooling layers. The LSTM layers obtain the flattened feature maps, which are then used to extract sequence information and temporal dependencies. To obtain the final predictions, fully connected (dense) layers process the output from the LSTM layers.

2.2.2.2. *Bidirectional LSTM (B-LSTM)*

B-LSTM is a kind of LSTM that improves model performance on sequence-based challenges. Bidirectional long-short term memory (Bi-LSTM) is the technique of allowing any neural network to store sequence information in both directions, forward and backward. Bidirectional LSTMs train two instead of one LSTM on the input sequence in cases where all timesteps of the input sequence are known. The first is the original input sequence, and the second is a reversed replica of the original input sequence. This may offer more context to the network, resulting in quicker and more complete learning model.

2.2.2.3. *Vanilla LSTM*

A basic kind of RNN, called vanilla LSTM, efficiently learns and remembers long-term relationships in sequential data, therefore solving the limitations of traditional RNNs. This is made possible by the distinctive cell structure and gating mechanism of LSTM networks, which regulate the information flow.

2.3. *Performance evaluation*

DL-based model LSTMs are valuable tools for weather nowcasting due to their ability to capture complex temporal relationships and adapt to evolving weather patterns. They enhance the performance and reliability of short-term weather predictions. Three different variants of LSTM, namely CNN-LSTM, B-LSTM, and V-LSTM, have been used. All of the tests were run across 50 epochs using the Adam Optimizer with a window size of 4 and a batch size of 2. In the experiments, 70% of the data set was used for training. After completing the training step, the remaining 30% data is used for testing. In this study, the entire satellite image is not predicted directly due to the very large data volume. Therefore, the original image is divided into randomly selected smaller regions of sizes 5 × 5, 20 × 20, and 50 × 50 pixels. This strategy reduces computational complexity and allows the model to effectively learn spatiotemporal patterns at different spatial scales for predicting future satellite data. For evaluating the performance of LSTM models on a certain testing set, two evaluation measures are computed over the test samples: the mean of absolute errors (MAE) and the normalized mean of absolute error (NMAE).

2.3.1. *Mean of absolute errors*

The Mean Absolute Error (MAE) is a measure of the average magnitude of errors between the predicted and actual value, without considering the direction of the errors.

Let the image size be $H \times W$, y_{ij} is the actual pixel value, and $\bar{y}_{ij}$ is the predicted value. The Mean Absolute Error (MAE) is then calculated as:

$$MAE = \frac{1}{\mathrm{H} \times \mathrm{W}} \sum_{i=1}^{H} \sum_{j=1}^{W} \left| y_{ij} - \bar{y}_{ij} \right| \quad (7)$$

2.3.2. *Normalized mean of absolute error*

The NMAE represents the normalized MAE obtained by dividing the MAE value by the range of the predicted output (1024 in our case) and is expressed as a percentage. The NMAE is then calculated as:

$$NMA = \frac{MAE}{1024} \quad (8)$$

The MAE and NMAE are used to measure the accuracy of a prediction model. A lower MAE and NMAE value indicate smaller prediction errors and, therefore, better model performance.

3. Results and discussion

This section provides the results of LSTM models. The satellite image has a total of 1618 X 1616 pixels in each image. In this research, the LSTM models are applied to randomly split small pixels of an image, like 5X5, 20X20, and 50X50 pixels, and the results are presented in Tables 1, 3, and 5. The particular pixels of the image are denoted as 4 km of data, which means we predict 25 km, 400 km, and 40000 km of data.

Tables 1, 3, and 5 present the predictions of TIR-1 data for durations of 30-minute, 1- hour, 1.5-hour, and 2-hour using CNN-LSTM, B-LSTM, and V-LSTM models. In these tables, block 1 contains the image's total image

TABLE 1

Result Table using the CNN-LSTM on TIR-1 Data

Image size	X-axis	Y-axis	Training		30-minute prediction		1-hour prediction		1.5-hour prediction		2-hour prediction	
			MAE	NMAE	MAE	NMAE	MAE	NMAE	MAE	NMAE	MAE	NMAE
50x50	380	1430	35.94	3.51	21.20	2.07	28.44	2.78	42.09	4.11	57.18	5.58
20x20	380	1430	27.75	2.71	40.41	3.95	54.09	5.28	74.95	7.32	91.07	8.89
5x5	380	1430	30.07	2.94	59.03	5.76	60.08	5.87	116.12	11.34	119.34	11.65
50x50	900	400	2.94	0.29	3.63	0.35	5.44	0.53	8.08	0.79	9.72	0.95
20x20	900	400	3.73	0.36	3.73	0.36	4.80	0.47	6.48	0.63	7.12	0.70
5x5	900	400	3.85	0.38	3.31	0.32	4.17	0.41	5.50	0.54	6.34	0.62
50x50	1000	500	3.04	0.30	4.38	0.43	4.36	0.43	6.76	0.66	8.23	0.80
20x20	1000	500	3.63	0.35	3.62	0.35	3.55	0.35	6.45	0.63	7.13	0.70
5x5	1000	500	5.08	0.50	4.57	0.45	5.36	0.52	8.15	0.80	8.72	0.85
50x50	1000	800	3.04	0.30	4.38	0.43	4.36	0.43	6.76	0.66	8.23	0.80
20x20	1000	800	9.75	0.95	17.46	1.70	20.50	2.00	30.46	2.97	37.93	3.70
5x5	1000	800	5.42	0.53	5.02	0.49	5.60	0.55	8.19	0.80	9.18	0.90
50x50	1200	1110	29.00	2.83	26.84	2.62	34.11	3.33	42.99	4.20	50.33	4.92
20x20	1200	1110	11.13	1.09	11.88	1.16	11.61	1.13	13.40	1.31	14.59	1.43
5x5	1200	1110	5.72	0.56	4.95	0.48	6.37	0.62	8.00	0.78	9.64	0.94
Average			12.01	1.17	14.29	1.40	16.85	1.65	25.63	2.50	29.65	2.90

TABLE 2

Difference between the actual image brightness temperature in Celsius and the predicted image brightness temperature in Celsius using the CNN-LSTM model (in %)

Image size	X-axis	Y-axis	30-minute prediction		1-hour prediction		1.5-hour prediction		2-hour prediction	
			0 to 2 degree	Other degree	0 to 2 degree	Other degree	0 to 2 degree	Other degree	0 to 2 degree	Other degree
50x50	380	1430	28.6	71.4	21.84	78.16	15.8	84.2	12.04	87.96
20x20	380	1430	28.75	71.25	19.25	80.75	12.75	87.25	12.25	87.75
5x5	380	1430	8	92	12	88	12	88	4	96
50x50	900	400	100	0	100	0	99.88	0.12	99.8	0.2
20x20	900	400	100	0	100	0	100	0	99.75	0.25
5x5	900	400	100	0	100	0	100	0	100	0
50x50	1000	500	100	0	100	0	99.84	0.16	99.56	0.44
20x20	1000	500	100	0	100	0	99.75	0.25	99.5	0.5
5x5	1000	500	100	0	100	0	100	0	100	0
50x50	1000	800	100	0	100	0	99.84	0.16	99.56	0.44
20x20	1000	800	100	0	100	0	99.75	0.25	99.75	0.25
5x5	1000	800	96	4	96	4	72	28	72	28
50x50	1200	1110	71.72	28.28	64.04	35.96	59.76	40.24	57.36	42.64
20x20	1200	1110	90	10	89.5	10.5	89.5	10.5	88	12
5x5	1200	1110	100	0	100	0	96	4	96	4

TABLE 3

Result Table using the B-LSTM on TIR-1 Data (60-minute)

Image size	X-axis	Y-axis	Training		30-minute prediction		1-hour prediction		1.5-hour prediction		2-hour prediction	
			MAE	NMAE	MAE	NMAE	MAE	NMAE	MAE	NMAE	MAE	NMAE
50x50	380	1430	28.71	2.80	33.57	3.28	38.25	3.74	50.59	4.94	66.09	6.45
20x20	380	1430	26.26	2.56	53.85	5.26	69.47	6.78	95.53	9.33	113.95	11.13
5x5	380	1430	24.98	2.44	80.48	7.86	87.56	8.55	147.46	14.40	154.80	15.12
50x50	900	400	2.14	0.21	3.13	0.31	4.75	0.46	6.63	0.65	7.89	0.77
20x20	900	400	2.41	0.24	2.48	0.24	3.12	0.30	4.32	0.42	4.50	0.44
5x5	900	400	1.74	0.17	1.19	0.12	1.35	0.13	1.42	0.14	1.27	0.12
50x50	1000	500	2.31	0.23	3.83	0.37	3.72	0.36	5.35	0.52	6.56	0.64
20x20	1000	500	2.31	0.23	2.14	0.21	2.04	0.20	4.18	0.41	5.16	0.50
5x5	1000	500	2.49	0.24	2.52	0.25	2.90	0.28	6.22	0.61	6.37	0.62
50x50	1000	800	7.66	0.75	24.58	2.40	28.69	2.80	38.36	3.75	51.17	5.00
20x20	1000	800	6.76	0.66	16.21	1.58	18.18	1.78	22.63	2.21	26.68	2.61
5x5	1000	800	9.24	0.90	13.64	1.33	20.80	2.03	24.94	2.44	29.64	2.89
50x50	1200	1110	20.85	2.04	31.82	3.11	45.61	4.45	52.96	5.17	60.18	5.88
20x20	1200	1110	8.24	0.80	11.77	1.15	11.30	1.10	11.29	1.10	10.67	1.04
5x5	1200	1110	3.75	0.37	3.34	0.33	4.13	0.40	4.71	0.46	5.02	0.49
Average			9.99	0.98	18.97	1.85	22.79	2.23	31.77	3.10	36.66	3.58

TABLE 4

Difference between the actual image brightness temperature in Celsius and the predicted image brightness temperature in Celsius using the B-LSTM model (in %)

Image size	X-axis	Y-axis	30-minute prediction		1-hour prediction		1.5-hour prediction		2-hour prediction	
			0 to 2 degree	Other degree	0 to 2 degree	Other degree	0 to 2 degree	Other degree	0 to 2 degree	Other degree
50x50	380	1430	11.48	88.52	10.08	89.92	7.76	92.24	6.6	93.4
20x20	380	1430	7.5	92.5	4.5	95.5	3.75	96.25	3.5	96.5
5x5	380	1430	0	100	0	100	0	100	8	92
50x50	900	400	100	0	100	0	99.88	0.12	99.72	0.28
20x20	900	400	100	0	99.75	0.25	99.75	0.25	99.75	0.25
5x5	900	400	100	0	100	0	100	0	100	0
50x50	1000	500	100	0	99.92	0.08	99.8	0.2	99.52	0.48
20x20	1000	500	100	0	100	0	100	0	100	0
5x5	1000	500	100	0	100	0	100	0	100	0
50x50	1000	800	93.44	6.56	88.32	11.68	84.32	15.68	75	25
20x20	1000	800	99.25	0.75	95	5	86.5	13.5	75.5	24.5
5x5	1000	800	100	0	96	4	100	0	80	20
50x50	1200	1110	61.64	38.36	49.12	50.88	46.6	53.4	46.16	53.84
20x20	1200	1110	88.5	11.5	90.25	9.75	91	9	90.25	9.75
5x5	1200	1110	100	0	100	0	100	0	100	0

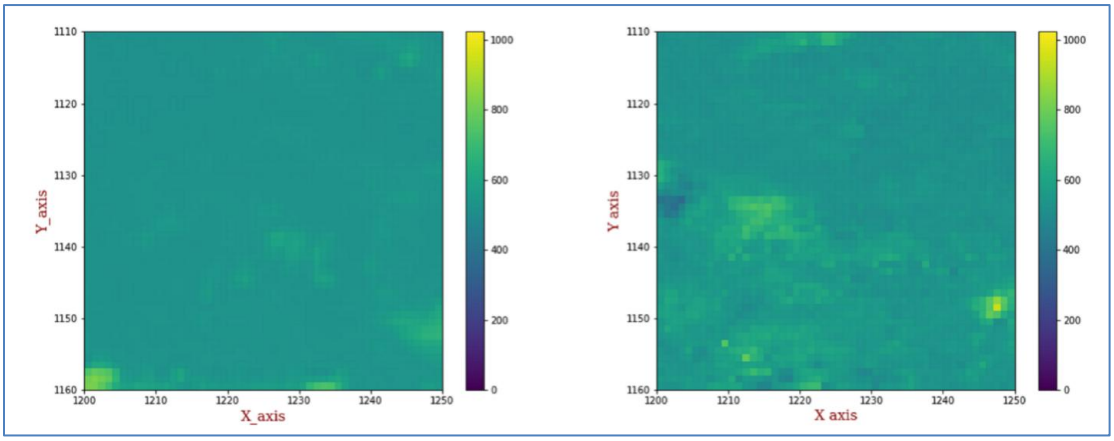

Fig. 3. Comparison of Original and Predicted Images using the CNN-LSTM Model (50x50 pixels, X-axis: 1200, Y-axis: 1110)

size in pixels (X-axis and Y-axis). The second block presents the X-axis of the selected image; the third block presents the Y-axis of the image; the fourth block presents the training result (MAE, NMAE); and the fifth to eighth block presents the 30-minute, 1-hour, 1.5-hour, and 2-hour prediction results (MAE, NMAE).

Tables 2, 4, and 6 present the difference between the actual image brightness temperature in Celsius and the predicted image brightness temperature in Celsius using CNN-LSTM, B-LSTM, and V-LSTM models on TIR-1 data for durations of 30-minute, 1-hour, 1.5-hour, and 2-hour. In these tables, block 1 contains the image's total image size in pixels (X-axis and Y-axis). The second block presents the X-axis of the selected image; the third block presents the Y-axis of the image; the fourth block presents the difference between the actual image brightness temperature in Celsius and the predicted image brightness temperature in Celsius on training data (0 to 2 degree, Other degree); and the fifth to eighth block presents the difference between the actual image brightness temperature in Celsius and the predicted image brightness temperature in Celsius of 30-minute, 1-hour, 1.5-hour, and 2-hour on testing data(0 to 2 degree, Other degree).

The CNN-LSTM models shown in Table 1 demonstrate that the results provided the best MAE and NMAE values for satellite image prediction of the TIR-1 image. The training results yielded an overall average MAE of 12.01% and an average NMAE of 1.17%. We achieved an average of 14.29% of MAE and an average of 1.40% of NMAE for 30-minute of satellite image prediction, 16.85% of an average MAE and 1.65% of an average NMAE for 1-hour of satellite image prediction, 25.63% of an average MAE and 2.50% of an average NMAE for 1.5-hour of satellite image prediction, and 29.65% of an average MAE and 2.90% of an average NMAE for 2-hour of satellite image prediction. The result shows excellent performance of CNN-LSTM models.

The result of the B-LSTM models shown in Table 3 reveals that the proposed model provided the best MAE and NMAE values for satellite image prediction of the TIR-1 image. An overall average MAE of 9.99% and an average NMAE of 0.98% were obtained for training results. We achieved an average of 18.97% of MAE and an average of 1.85% of NMAE for 30-minute satellite image prediction; 22.79% of an average MAE and 2.23% of an average NMAE were obtained for 1-hour satellite image prediction; 31.77% of an average MAE and 3.10% of an average NMAE were obtained for 1.5-hour satellite image prediction; and 36.66% of an average MAE and 3.58% of an average NMAE were obtained for 2-hour satellite image prediction.

The result of the V-LSTM models shown in Table 5 indicates the best MAE and NMAE values for satellite image prediction of the TIR-1 image. The training results produced an overall average MAE of 10.94% and an average NMAE of 1.07%. We achieved an average of 19.28% of MAE and an average of 1.88% of NMAE for 30-minute of satellite image prediction; 23.31% of an average MAE and 2.28% of an average NMAE were obtained for 1-hour of satellite image prediction; 33.28% of an average MAE and 3.25% of an average NMAE were obtained for 1.5-hour of satellite image prediction; and 38.51% of an average MAE and 3.76% of an average NMAE were obtained for 2-hour of satellite image prediction.

Tables 1, 3, and 5 show that the CNN-LSTM model performs better compared to other models. Fig. 3 present the results of predicted satellite images. Fig. 3 represents the comparison of the original and predicted satellite image (50x50 pixels, X-axis: 1200, Y-axis: 1110).

TABLE 5

Result Table using the V-LSTM on TIR-1 Data

Image size	X-axis	Y-axis	Training		30-minute prediction		1-hour prediction		1.5-hour prediction		2-hour prediction	
			MAE	NMAE	MAE	NMAE	MAE	NMAE	MAE	NMAE	MAE	NMAE
50x50	380	1430	37.59	3.67	33.82	3.30	39.95	3.90	55.15	5.39	73.62	7.19
20x20	380	1430	26.60	2.60	53.51	5.23	69.88	6.82	96.79	9.45	116.24	11.35
5x5	380	1430	25.46	2.49	77.79	7.60	88.81	8.67	151.01	14.75	158.10	15.44
50x50	900	400	2.19	0.21	3.10	0.30	4.69	0.46	6.54	0.64	7.81	0.76
20x20	900	400	2.50	0.24	2.46	0.24	3.07	0.30	4.16	0.41	4.40	0.43
5x5	900	400	1.94	0.19	0.99	0.10	1.20	0.12	1.29	0.13	1.02	0.10
50x50	1000	500	2.25	0.22	3.87	0.38	3.60	0.35	5.18	0.51	6.21	0.61
20x20	1000	500	2.52	0.25	2.44	0.24	2.24	0.22	4.21	0.41	5.17	0.50
5x5	1000	500	3.55	0.35	3.45	0.34	3.07	0.30	5.89	0.58	6.09	0.59
50x50	1000	800	7.78	0.76	25.21	2.46	30.01	2.93	40.25	3.93	53.25	5.20
20x20	1000	800	6.54	0.64	18.91	1.85	22.77	2.22	29.66	2.90	36.74	3.59
5x5	1000	800	10.53	1.03	14.47	1.41	18.16	1.77	25.41	2.48	28.77	2.81
50x50	1200	1110	22.42	2.19	32.72	3.20	47.22	4.61	57.45	5.61	65.33	6.38
20x20	1200	1110	8.34	0.81	12.90	1.26	10.69	1.04	11.77	1.15	10.19	0.99
5x5	1200	1110	3.82	0.37	3.57	0.35	4.24	0.41	4.39	0.43	4.77	0.47
Average			10.94	1.07	19.28	1.88	23.31	2.28	33.28	3.25	38.51	3.76

TABLE 6

Difference between the actual image brightness temperature in Celsius and the predicted image brightness temperature in Celsius using the V-LSTM model (in %)

Image size	X-axis	Y-axis	30-minute prediction		1-hour prediction		1.5-hour prediction		2-hour prediction	
			0 to 2 degree	Other degree	0 to 2 degree	Other degree	0 to 2 degree	Other degree	0 to 2 degree	Other degree
50x50	380	1430	10.56	89.44	9.92	90.08	7.4	92.6	7.64	92.36
20x20	380	1430	5.5	94.5	5.5	94.5	4.75	95.25	4.25	95.75
5x5	380	1430	0	100	0	100	0	100	0	100
50x50	900	400	99.96	0.04	99.96	0.04	99.96	0.04	99.84	0.16
20x20	900	400	100	0	100	0	99.75	0.25	99.75	0.25
5x5	900	400	100	0	100	0	100	0	100	0
50x50	1000	500	99.96	0.04	99.88	0.12	99.8	0.2	99.76	0.24
20x20	1000	500	100	0	100	0	100	0	99.75	0.25
5x5	1000	500	100	0	100	0	100	0	100	0
50x50	1000	800	93.16	6.84	87.84	12.16	82.56	17.44	74.2	25.8
20x20	1000	800	99.25	0.75	97.5	2.5	95	5	93.25	6.75
5x5	1000	800	100	0	100	0	100	0	96	4
50x50	1200	1110	60.52	39.48	48.48	51.52	46.76	53.24	46.12	53.88
20x20	1200	1110	88	12	91.25	8.75	90.5	9.5	90.75	9.25
5x5	1200	1110	96	4	100	0	100	0	100	0

TABLE 7

Comparison of average MAE and NMAE between the CNN-LSTM, B-LSTM, and V-LSTM models for 30-minute, 1-hour, 1.5-hour, and 2-hour of predication in TIR-1 data

Prediction Time	CNN-LSTM	CNN-LSTM	B-LSTM	B-LSTM	V-LSTM	V-LSTM
	MAE	NMAE	MAE	NMAE	MAE	NMAE
30-minute	14.29%	1.40%	18.97%	1.85%	19.28%	1.88%
1-hour	16.85%	1.65%	22.79%	2.23%	23.31%	2.28%
1.5-hour	25.63%	2.50%	31.77%	3.10%	33.28%	3.25%
2-hour	29.65%	2.90%	36.66%	3.58%	38.51%	3.76%

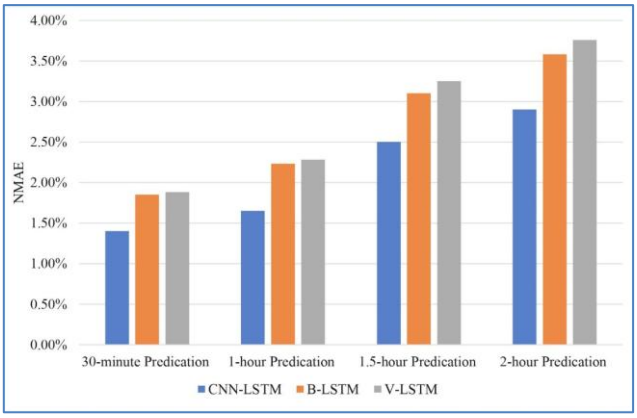

Fig. 4. Comparison between CNN-LSTM, B-LSTM, and V-LSTM models in terms of NMAE for 30-minute, 1-hour, 1.5-hour, and 2-hour of predication in TIR-1 data

Fig. 3 show the comparison of the original and predicted images by the CNN-LSTM model. The CNN-LSTM model has remarkable performance in image prediction tasks, according to the findings. The model is very successful and has potential applications requiring precise image reconstruction or prediction, as shown by the high degree of visual and quantitative similarity between the original and predicted images.

Table 7 shows the comparison of average MAE and NMAE between the CNN-LSTM, B-LSTM, and V-LSTM models for 30-minute, 1-hour, 1.5-hour, and 2-hour of predication in TIR-1 data, and Fig. 4 represents the comparison between CNN-LSTM, B-LSTM, and V-LSTM models in terms of NMAE for 30-minute, 1-hour, 1.5-hour, and 2-hour of predication in TIR-1 data. In Table 7, it is clearly shown that the CNN-LSTM model performed very well compared to B-LSTM and V-LSTM in terms of MAE and NMAE. In Fig. 4, the CNN-LSTM model shows outstanding prediction accuracy for fewer time intervals, especially at 30 minutes. On the other hand, the accuracy decreases with an increasing forecast interval, indicating the limitations of the model over longer times.

The experimental results demonstrate that the proposed LSTM-based framework successfully achieves the stated objective by accurately predicting future INSAT-3DR TIR-1 satellite images across multiple lead times.

4. Conclusions

This research presents a long-short-term memory (LSTM) deep learning model, a LSTM model designed for predicting future satellite images using historical satellite imagery, with a specific focus on weather nowcasting. It uses recent, original satellite data to predict future satellite data. Satellite TIR-1 data were used in the experiments that utilized the satellite data obtained by the INSAT3DR satellite. In the experiments, we initially divided the original image into smaller areas, such as 5x5, 20x20, and 50x50 pixels, in order to predict future satellite images. In these smaller areas, we used three different types of LSTM models: CNN-LSTM, B-LSTM, and V-LSTM, to predict future satellite images. We achieved a minimum average normalized mean of absolute errors (NMAE) of 1.40% on the CNN-LSTM model compared to other LSTM models, demonstrating the effectiveness of the CNN-LSTM model. It is worth noting that our approach outperforms all but the LSTM-based methods, which exhibit significantly lower mean absolute error (MAE) values. In this study, the objective of developing an LSTM-based nowcasting framework for INSAT-3DR satellite imagery has been successfully achieved. While our model offers advantages in terms of simplicity, there is still scope for improvement. To address this, we plan to explore lightweight LSTM-based models tailored to this problem. The future work aims to strike a balance between ease of training and improved performance compared to non-recurrent approaches, and could focus on improving long-term prediction accuracy and reducing MAE for extended intervals. Also, the future work will explore the integration of multiple INSAT-3DR spectral channels, including both infrared and visible bands, to potentially improve the accuracy and reliability of short-term weather nowcasting.

Authors' contributions

Amit Saxena: Conceptualization, and manuscript revision (*email: amitsaxena65@rediffmail.com*).
Damodar Patel: Code run, writing - original manuscript, and analysis (*email: damodarpatel7497@gmail.com*).
Abhishek Dubey: Manuscript revision, and validation. (*email: abhishekdubey003@gmail.com*)
Pratiksha Dubey: Conceptualization, analysis and editing (*email: pratikshadubey2207@gmail.com*).
Pankaj Kumar: Validation, and analysis (*email: kumarpankaj2794@gmail.com*).
Ashim Kumar Mitra: Conceptualization, Manuscript revision and Supervision (*email: ashimmitra@gmail.com*).

Disclaimer: The contents and views expressed in this research article are the views of the authors and do not necessarily reflect the views of the organizations they belong to.

References

Agrawal, S., Barrington, L., Bromberg, C., Burge, J., Gazen, C., and Hickey, J., 2019, "*Machine Learning for Precipitation Nowcasting from Radar Images*", arXiv preprint arXiv, **1912**, 12132. doi: https://doi.org/10.48550/arXiv.1912.12132.

Bharill, N., Tiwari, A., Malviya, A., Patel, O. P., Gupta, A., Puthal, D., Saxena, A., and Prasad, M., 2020, "Fuzzy knowledge based performance analysis on big data", *Neurocomputing*, **389**, 218-228. doi: https://doi.org/10.1016/j.neucom.2018.10.088.

Berthomier, L., Pradel, B., and Perez, L., 2020, "Cloud Cover Nowcasting with Deep Learning", *2020 10th International Conference on Image Processing Theory, Tools and Applications, IPTA 2020*, 1-6. doi: https://doi.org/10.1109/IPTA50016.2020.9286606.

Dubey, V. K., and Saxena, A. K., 2017, "A cosine-similarity mutual-information approach for feature selection on high dimensional datasets", *Journal of Information Technology Research*, 10, 1, 15–28. doi: https://doi.org/10.4018/JITR.2017010102.

Gao, G., Wang, C., Wang, J., Lv, Y., Li, Q., Ma, Y., Zhang, X., Li, Z., and Chen, G., 2023, "CNN-Bi-LSTM: A Complex Environment-Oriented Cattle Behavior Classification Network Based on the Fusion of CNN and Bi-LSTM", *Sensors*, 23, 18, 7714. doi: https://doi.org/10.3390/s23187714.

Giri, R. K., Prakash, S., Yadav, R., & Saikrishnan, K. C., 2023, "INSAT geostationary meteorological satellite program and current meteorological data processing system for INSAT-3D/3DR/3DS at India Meteorological Department", *Vayumandal*, **49**, 1, 11-28. doi: https://vayumandal.imetsociety.org/index.php/Vayumandal/article/view/20.

INSAT-3DR Meteorological and Oceanographic Satellite Data Archival Centre. (n.d.). Retrieved May 24, 2024. from https://www.mosdac.gov.in/insat-3dr.

Ionescu, V. S., Czibula, G., & Mihuleț, E., 2021, "DeePS at: A deep learning model for prediction of satellite images for nowcasting purposes", *Procedia Computer Science*, **192**, 622-631. doi: https://doi.org/10.1016/j.procs.2021.08.064.

Kamber, M., Han, J., and Pei, J., 2006, Data Mining Concepts and Techniques (2nd ed.). Morgan Kaufmann.

Kotsuki, S., Kurosawa, K., Otsuka, S., Terasaki, K., and Miyoshi, T., 2019, "Global precipitation forecasts by merging extrapolation-based nowcast and numerical weather prediction with locally optimized weights", *Weather and Forecasting*, **34**, 3, 701-714. doi: https://doi.org/10.1175/WAF-D-18-0164.1.

Kumar, A., Islam, T., Sekimoto, Y., Mattmann, C., and Wilson, B., 2020, "ConvCast: An embedded convolutional LSTM based architecture for precipitation nowcasting using satellite data", *PLoS ONE*, **15**, 3, e0230114. doi: https://doi.org/10.1371/journal.pone.0230114.

Lebedev, V., Ivashkin, V., Rudenko, I., Ganshin, A., Molchanov, A., Ovcharenko, S., Grokhovetskiy, R., Bushmarinov, I., and Solomentsev, D., 2019, "Precipitation nowcasting with satellite imagery. *Proceedings of the ACM SIGKDD International Conference on Knowledge Discovery and Data Mining*, 2680-2688. doi: https://doi.org/10.1145/3292500.3330762.

Otsuka, S., Kotsuki, S., and Miyoshi, T., 2016, "Nowcasting with data assimilation: A case of global satellite mapping of precipitation", *Weather and Forecasting*, **31**, 5, 1409-1416. doi: https://doi.org/10.1175/WAF-D-16-0039.1.

Sherstinsky, A., 2020, "Fundamentals of Recurrent Neural Network (RNN) and Long Short-Term Memory (LSTM) network", *Physica D: Nonlinear Phenomena*, **1**, 404, 132306. doi: https://doi.org/10.1016/j.physd.2019.132306.

Shukla, B. P., Kishtawal, C. M., and Pal, P. K., 2013, "Prediction of satellite image sequence for weather nowcasting using cluster-based spatiotemporal regression", *IEEE transactions on geoscience and remote sensing*, **52**, 7, 4155-4160. doi: https://doi.org/10.1109/TGRS.2013.2280094.

Shukla, B. P., Pal, P. K., and Joshi, P. C., 2010, "Extrapolation of sequence of geostationary satellite images for weather nowcasting", *IEEE Geoscience and Remote Sensing Letters*, **8**,2,216-219. doi: https://doi.org/10.1109/LGRS.2010. 2060311.

Singh, N., Shukla, B. P., Kaushik, N., Varma, A. K., Mitra, A. K., and Bhan, S. C., 2023, "Validation of INSAT-3D/3DR based nowcasting rain occurrences for heavy rainfall using Hydro-Estimator product", *Advances in Space Research*, **72**, 6, 2185-2194. doi: https://doi.org/10.1016/j.asr.2023.05.030.

Son, L. H., and Thong, P. H., 2017, Some novel hybrid forecast methods based on picture fuzzy clustering for weather nowcasting from satellite image sequences", *Applied Intelligence*, **46**, 1, 1-15. doi: https://doi.org/10.1007/s10489-016-0811-1.

Venkatesan, D., Kannan, S. K., Arif, M., Atif, M., and Ganeshan, A., 2022, "Sentimental Analysis of Industry 4.0 Perspectives Using a Graph-Based Bi-LSTM CNN Model", *Mobile Information Systems*, 1, 5430569. doi: https://doi.org/10.1155/2022/5430569.

Wang, J., Xu, Y., Yang, L., Wang, Q., Yuan, J., and Wang, Y., 2020, "Data assimilation of high-resolution satellite rainfall product improves rainfall simulation associated with landfalling tropical cyclones in the Yangtze River Delta", *Remote Sensing*, **12**, 2, 276. doi: https://doi.org/10.3390/rs12020276.

Zhu, Q., Wang, C., Jin, W., Ren, J., and Yu, X., 2024, "Deep Transfer Learning Based on LSTM Model for Reservoir Flood Forecasting", *International Journal of Data Warehousing and Mining*, **20**, 1, 1–17. doi: https://doi.org/10.4018/IJDWM.338912.